Circular dichroism experiments at the L edge of magnetic transition metals enabled by elliptically polarized pulses from a seeded free-electron laser

C. Spezzani, A. Ravindran, E. Allaria, L. Badano, R. Bhardwaj, A. Brynes, P. Capaldo, A. Caretta, P. Cinquegrana, A. Contillo, et al.

Circular dichroism experiments at the L edge of magnetic transition metals enabled by elliptically polarized pulses from a seeded free-electron laser

C. Spezzani,[1] A. Ravindran,[2] E. Allaria,[1] L. Badano,[1] R. Bhardwaj,[1] A. Brynes,[1] P. Capaldo,[2] A. Caretta,[1] P. Cinquegrana,[1] A. Contillo,[1] M. Danailov,[1] A. Demidovich,[1] S. Dal Zillo,[2] G. De Ninno,[1,3,*] B. Diviacco,[1] G. Kurdi,[1] D. Garzella,[1] G. Geloni,[4] L. Giannessi,[1,5] S. Laterza,[1] M. Manfredda,[1] I. Nikolov,[1] M. Pancaldi,[1,6] M. Pasqualetto,[1] E. Pedersoli,[1] G. Penco,[1] G. Perosa,[1,7] M. Prica,[1] L. Raimondi,[1] P. Rebernik Ribič,[1] C. Scafuri,[1] P. Sigalotti,[1] A. Simoncig,[1] F. Sottocorona,[1,7] S. Spampinati,[1] P. Susnjar,[1] F. Tripaldi,[1] M. Trovò,[1] M. Zangrando,[1,8] F. Capotondi,[1] N. Jaouen,[6,9] M. Malvestuto,[1] and M. Sacchi[9,10]

[1]*Elettra-Sincrotrone Trieste S.C.p.A., Trieste, Italy*

[2]*CNR IOM, S.S. 14 - km 163,5 in Area Science Park, 34149 Basovizza, Trieste, Italy*

[3]*University of Nova Gorica, Ajdovščina, Slovenia*

[4]*European XFEL, Holzkoppel 4, 22869 Schenefeld, Germany*

[5]*INFN LFN, Frascati, Italy*

[6]*Università Ca' Foscari, Venezia, Italy*

[7]*Università degli Studi di Trieste, Trieste, Italy*

[8]*Istituto Officina dei Materiali, Consiglio Nazionale delle Ricerche, 34149 Trieste, Italy*

[9]*Synchrotron SOLEIL, Saint Aubin, France*

[10]*INSP, UMR 7588 CNRS, Sorbonne Université, Paris, France*

We have generated elliptically polarized femtosecond pulses from a seeded free-electron laser (FEL) in the spectral range 700–800 eV and conducted demonstrative experiments based on magnetic circular dichroism, at the Fe L_3 edge. This was achieved by making use of the radiation produced at the third harmonic of the fundamental FEL wavelength λ. A planar radiator emits linearly polarized harmonics along the undulator axis, while a helical undulator produces off-axis harmonic radiation with circular polarization. However, off-axis circularly polarized light is characterized by a rather low flux and, as a result, it is unsuitable for most experiments that rely on circular dichroism. Here, we demonstrate that on-axis radiation with a substantial degree of circular polarization at $\lambda/3$ can be generated using a variable-polarization (APPLE-type) radiator, finely tuned in a hybrid-polarization mode. The experiments, which demonstrate the potential of the adopted configuration for magnetic dichroism studies, were carried out at the FERMI FEL facility in Trieste (Italy). These results pave the way to experiments at the $2p$-$3d$ resonances of the transition metals most relevant for magnetic studies (Fe, Co, Ni) and make it possible to envisage investigations, e.g., spectroscopic studies with different core-hole lifetimes, covering both the M (50–70 eV) and L (600–900 eV) edges, at the same seeded FEL source.

DOI: 10.1103/PhysRevB.00.004400

I. INTRODUCTION

The ability to control light polarization plays a crucial role in the study of the local symmetry of various materials, such as the lattice geometry of crystals, the chirality of molecules, or the presence of atomic magnetic moments. The relative orientation between light polarization and symmetry axes can have a strong influence on the cross-section of the induced electronic transitions, affecting absorption and scattering processes. Furthermore, it is common to rely on the reversal of the helicity of circularly polarized radiation to distinguish between signals arising from the breaking of local symmetry and those originating from the isotropic background. As a result, polarization-dependent spectroscopy using synchrotron radiation has emerged as a powerful tool for investigating the electronic and magnetic properties of matter [1–5]. The extension to dynamic studies with high temporal resolution has taken advantage of the time structure of the different available x-ray sources, from synchrotrons [6,7] to high-harmonic generation in gases [8,9], offering complementary technical capabilities in terms of, e.g., time resolution, repetition rate, flux, and polarization control.

The advent of free-electron lasers (FELs) has revolutionized spectroscopy [10–14], scattering [15–18], and diffraction [19,20] studies due to their significantly enhanced photon brilliance compared with conventional sources. Indeed, FELs offer control over both the temporal duration and spectral bandwidth of the emitted light, opening avenues in these research fields. The effectiveness of these studies is further augmented by the availability of well-defined and easily adjustable light polarization [20,21] as well as of detectors capable of sensing polarized photons in the x-ray spectral region [22,23]. In a FEL, light is emitted when a relativistic

*Contact author: giovanni.deninno@elettra.eu

electron beam passes through the static and periodic magnetic field of an undulator. Like synchrotron radiation, FEL emission occurs at a specific fundamental wavelength [20] $\lambda = \lambda_u/(2\gamma^2)(1 + K^2)$, where λ_u is the undulator period, γ represents the electron-beam relativistic energy, and K is the deflection parameter, proportional to the undulator field strength, as well as at the harmonics $\lambda_n = \lambda/n$, where $n > 1$ is an integer [24]. The power emitted at low-order harmonics ($n \leqslant 5$) is usually a significant fraction, ~1%, of that emitted at the fundamental wavelength. This process, known as non-linear harmonic generation (NHG) [25–29], can be harnessed to extend the wavelength range of the FEL toward shorter values, corresponding to higher photon energies.

It is known that the use of planar undulators results in on-axis linearly polarized emission at odd harmonics of the fundamental, while even harmonics are emitted off-axis [30]. Conversely, circularly polarized harmonic radiation from helical undulators is distributed off-axis [31,32]. In Ref. [33], a quantitative estimate of the off-axis harmonic intensity has been performed. The results indicate that collecting off-axis circularly polarized emission leads to a reduction in flux of several (~6 for the configuration discussed in this paper) orders of magnitude. Consequently, such radiation is unsuitable for experiments that aim at utilizing circular dichroism as a diagnostic tool to investigate the properties of matter samples.

In Ref. [34], the authors demonstrated the generation of on-axis elliptically polarized nonlinear harmonics using variable-polarization (APPLE-type) undulators, allowing seamless transitions between planar and helical configurations. This experiment was conducted on a prototype FEL [35] at a relatively long wavelength $\lambda = 195$ nm. The results revealed the potential for a hybrid undulator configuration to produce on-axis radiation, with substantial circular polarization and high intensity. However, critical questions remained regarding the extension of the technique into the VUV and x-ray spectral regions using a high-gain FEL as well as its possible use in probing the dichroic properties of matter.

In this paper, we address these questions, focusing on the generation of coherent elliptically polarized nonlinear harmonics within the 700–800 eV spectral range, which cannot currently be obtained through fundamental emission in a seeded FEL. We note that the same technique could also be implemented in nonseeded FELs but at the cost of sacrificing longitudinal coherence, which may be essential for a wide range of dichroism studies. Two successful experiments were performed at the FERMI FEL [36], employing techniques based on circular dichroism at the Fe L_3 edge: static x-ray magnetic circular dichroism (XMCD) on a permalloy (Py) sample and time-resolved x-ray resonant magnetic scattering (XRMS) on a synthetic antiferromagnet (SAFM). Our results, combined with those presented in Ref. [29], underscore the value of NHG as a technique for extending the capabilities of FEL user facilities.

The paper is organized as follows. Section II outlines the FEL scheme for generating on-axis third harmonic radiation with elliptical polarization. Section III presents the results of static XMCD and time-resolved XRMS demonstrative experiments. Finally, Sec. IV is dedicated to conclusions and offers insights into future perspectives.

II. FEL SCHEME

The operational principle of the FERMI FEL is shown in Fig. 1(a). The electron beam reaches the radiator entrance, where FEL emission occurs at the fundamental wavelength of $\lambda = 5.2$ nm and at its third harmonic $\lambda/3 = 1.75$ nm (708 eV). The FEL process is triggered by a spatial modulation of electrons, both at the fundamental and third harmonic, called *bunching*, which is initiated by the interaction of electrons with an external seed laser, at an earlier stage of the FEL process [37]. During the emission process, the bunching at the fundamental wavelength intensifies, amplifying light emission at λ. This amplification contributes to increased bunching at the fundamental and its harmonics, entering a nonlinear regime and sustaining harmonic gain. The radiator consists of six variable-polarization (APPLE-type) undulators, separated by drift regions.

Unlike standard (fixed-polarization) undulators, in APPLE-type undulators [38], the magnet arrays generating the magnetic field can be shifted longitudinally relative to each other, as shown in Fig. 1(b). When the shift is zero, the magnetic field is confined in the vertical (y, z) plane (i.e., $B_x = 0$ and $B_y \neq 0$) and forms a sinusoidal pattern, indicated by the dashed line in Fig. 1(b). Electrons traveling through the undulator (along the z direction) are deflected in the horizontal (x, z) plane, resulting in linear horizontal polarization of the emitted radiation. This configuration is known as the *planar configuration*. By adjusting the relative position of the magnet arrays, it becomes possible to introduce a horizontal component to the magnetic field B_x. When the shift between the two components is $\lambda_u/4$, the strength of B_x equals that of B_y, and the resulting magnetic field forms a helix with a period of λ_u, shown as the solid line in Fig. 1(b). In this scenario, the electron trajectory follows a helical path, and the emitted radiation becomes circularly polarized. Intermediate values of the ratio B_x/B_y result in elliptically polarized emission.

For the experiment conducted, all undulators were initially configured in right circular polarization (i.e., no harmonic on-axis signal). To obtain a nonzero harmonic on-axis signal with elliptical polarization, the first four undulators were maintained in circular polarization, and the phase of the last two, i.e., the ratio B_x/B_y, was set to an intermediate optimum value.

Setting the first part of the radiator in circular polarization enables maximizing the coupling between electrons and the undulator field, thereby enhancing bunching at both the fundamental wavelength and its harmonics. However, we did not observe any critical dependence of the results reported in the remaining part of this paper on the ratio between the number of sections tuned either in circular or hybrid-polarization mode.

A preliminary estimate of the optimum value of B_x/B_y in the radiator sections tuned in hybrid-polarization mode was derived by plotting the theoretical trend of the relative Stokes parameters of the spontaneous radiation produced by a variable-polarization undulator, specifically M/I and S/I [39]. Here, I is the total light intensity, M represents the fraction of intensity linearly polarized in the coordinate system defined in Fig. 1(b), and S is the fraction of intensity with circular

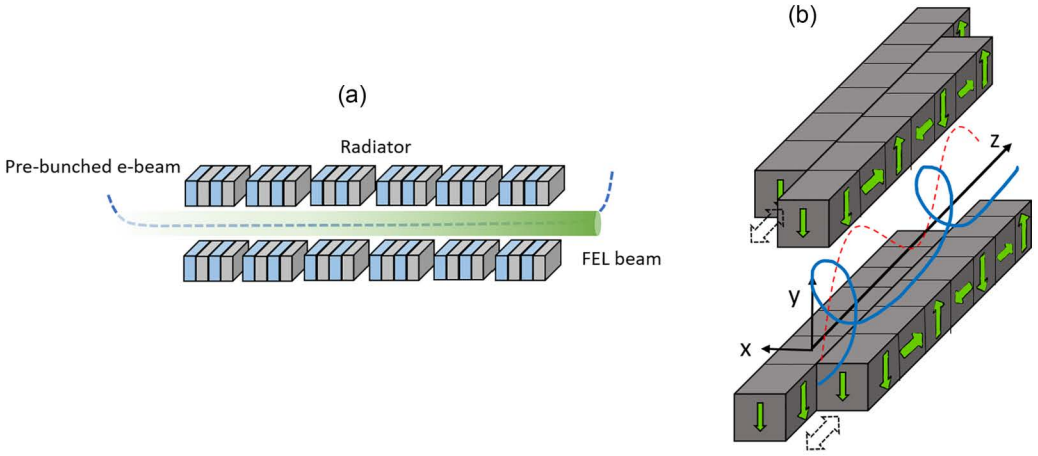

FIG. 1. (a) Free-electron laser (FEL) scheme. The electron beam, prebunched in an earlier stage of the process, arrives at the FEL radiator ready to emit radiation at the fundamental wavelength $\lambda = 5.2$ nm and at its third harmonic $\lambda/3 = 1.75$ nm (708 eV). The radiator is made of six independent modules, separated by drift sections. For the present experiment, the electron-beam properties are like those reported in Ref. [25]. (b) Schematic layout of a helical (APPLE type) undulator. The dashed red and solid blue lines indicate, respectively, the magnetic field generated by the undulator in linear and helical configurations.

polarization. The trend of these parameters as a function of B_x/B_y, reported in Fig. 2(a), offers insight into the polarization state of the emitted radiation [39]. When the polarization is fully linear horizontal, $M = I$ and $S = 0$, while for right circular polarization, $M = 0$ and $S = I$. As expected, the degree of circular polarization increases progressively, moving from the condition $B_x = 0$ to $B_x = B_y$. In Fig. 2(b), the measured intensity of the harmonic signal, collected over an area a few times larger than the beam size, is reported as a function of B_x/B_y. The same picture also shows the two components of the on-axis intensity $(I_z)_x$ and $(I_z)_y$ as well as the total on-axis intensity $I_z = (I_z)_x + (I_z)_y$, derived from first-principles calculations [39,40]. We remark that there is very good agreement between the measured and calculated intensities. As anticipated, starting from $B_x/B_y = 0$ (linearly polarized on-axis harmonic radiation), the signal weakens and eventually vanishes as the ratio increases, approaching circular polarization. This analysis highlights that the optimal conditions for conducting experiments to detect the dichroic properties of materials using elliptical polarization produced by NHG involve striking a balance between attaining the highest possible degree of circular polarization and maintaining a reasonable signal intensity. Comparing the outcomes presented in Figs. 2(a) and 2(b), it can be inferred that an appropriate B_x/B_y ratio falls within the range of 0.2–0.4. This corresponds to S/I values in the interval 0.3–0.6, indicating a circular polarization degree of 30–60%, with a reduction in the NHG on-axis signal not exceeding 30%. However, a significantly higher circular polarization degree can be achieved if the sample under investigation allows one to work with further reduced intensity.

III. NONLINEAR HARMONICS WITH ELLIPTICAL POLARIZATION AS A PROBE FOR CIRCULAR DICHROISM AT THE *L* EDGE OF MAGNETIC TRANSITION METALS

In this section, we report the results of two pilot experiments, which allowed us to demonstrate the use of the harmonic pulses generated by the technique illustrated in the

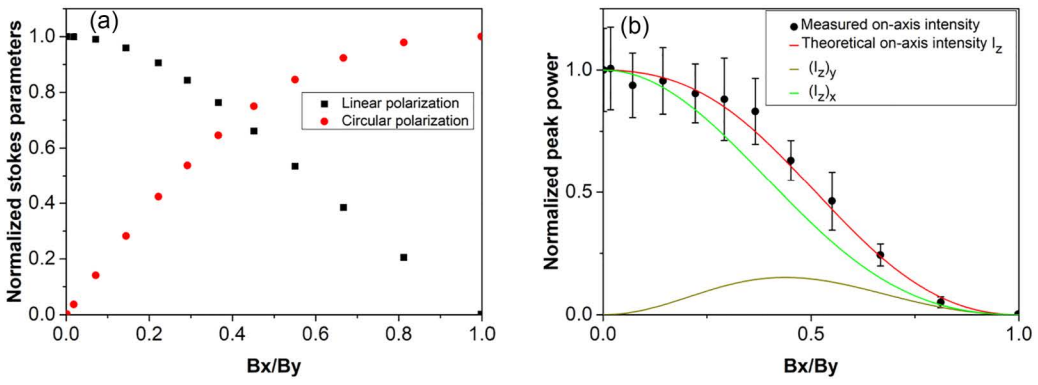

FIG. 2. (a) Predicted Stokes' parameters M/I and S/I for the third harmonic of spontaneous emission, as a function of the ratio B_x/B_y. (b) Measured (dots) and simulated harmonic free-electron laser (FEL) on-axis intensity I_z at $\lambda/3 = 1.75$ nm, as a function of B_x/B_y. Also shown are the components of the on-axis intensity $(I_z)_x$ and $(I_z)_y$, such that $I_z = (I_z)_x + (I_z)_y$.

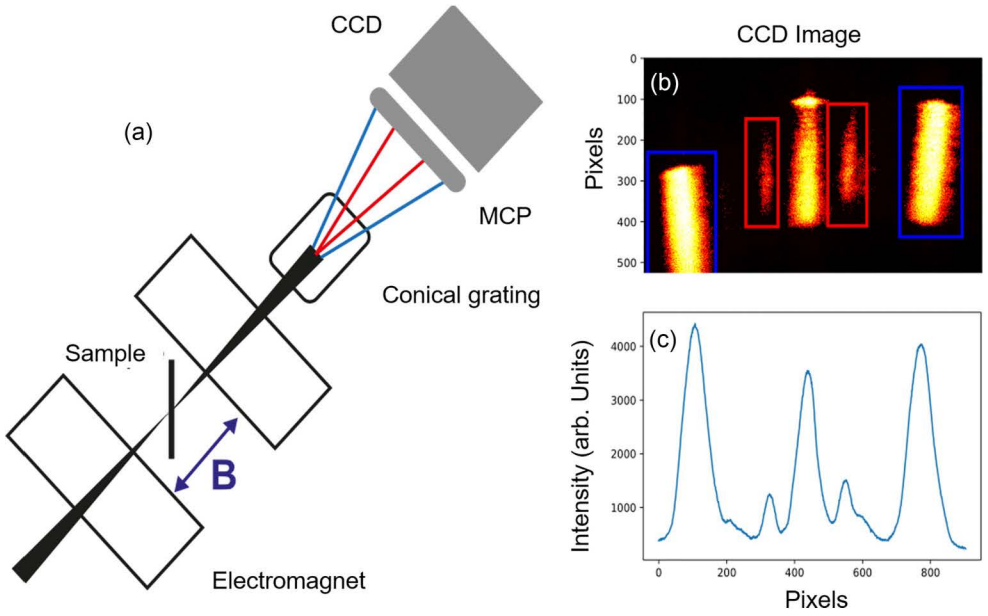

FIG. 3. Layout of the experimental setup at the MagneDyn beamline (top view). (a) The sample, a permalloy film [Fe(20 nm)Ni(80 nm)] deposited on 100-nm-thick SiN membranes, rotated at 45 ° relative to the impinging free-electron laser (FEL) radiation, is placed between the poles of an electromagnet. The magnetic field is aligned parallel to the FEL beam. Photons transmitted through the sample are diffracted by a conical grating, collected by a microchannel-plate (MCP) and visualized on a fluorescent screen by a charge-coupled device (CCD) camera. The spatially separated harmonic components are collected simultaneously for every FEL shot. An example of CCD image is presented in (b), where the first positive and negative diffraction orders of the fundamental emission and the third harmonic are highlighted in blue and red boxes, respectively. The nondiffracted zero order appears at the center. (c) Intensity of the zero order as well as that of the first and third harmonics, after full vertical binning of the image from the upper panel. Each energy point consists of the accumulation of 1000 FEL shots at 50 Hz, taken with reversed external magnetic fields saturating the sample. The dataset displayed in the figure is the average of three photon energy scans.

previous section, for probing both the static and dynamical magnetic properties of materials at the L edge of transition metal atoms, through circular dichroism. A direct comparison with the results obtained using fully circularly polarized synchrotron radiation allows us to quantify the degree of circular polarization carried by the FEL harmonic.

A. Measurement of dichroic contrast through XMCD

Static XMCD measurements were performed at the Fe-L_3 edge on a Py sample at the MagneDyn beamline of the FERMI FEL [41]. The experiment was performed in transmission geometry.

The sample is mounted on a sample holder and placed between the poles of an electromagnet. The externally applied magnetic field B is collinear with the FEL beam, as shown in Fig. 3(a). The sample is positioned at a 45 ° angle with respect to the normal incidence to the surface. This orientation was chosen because the samples have in-plane magnetization. In an XMCD experiment, to observe MCD contrast, a component of the magnetization must align with the wave vector of the incoming photon beam.

During the measurements, the magnetization of the Py sample was saturated by an external magnetic field. The photons transmitted through the sample were energy dispersed by a conical diffraction grating onto a microchannel plate detector, coupled to a charge-coupled device (CCD) camera. A typical single-shot image is reported in Fig. 3(b). A quantitative estimate of the third harmonic emission intensity can be obtained from the vertical binned image displayed in Fig. 3(c), and it amounts to ∼10 nJ. To identify the wavelength that yields the maximum magnetic contrast, the photon energy was scanned across the Fe-L_3 absorption edge by tuning the FEL wavelength, see Fig. 4(a). At FERMI, this tuning is achieved using an optical parametric amplifier to seed the FEL process. The XMCD signal plotted in Fig. 4, directly quantifying the sample magnetization, was obtained as $(I_+ - I_-)/(I_+ + I_-)$, where I_+ and I_- are the transmitted intensities for opposite values of the applied magnetic field. Each energy point consists of the accumulation of 1000 FEL shots at 50 Hz taken with reversed external magnetic fields saturating the sample. We took 23 photon energy points with 0.5 eV energy steps. The dataset displayed in the figure is the average of three photon energy scans.

The obtained shape of the absorption edge aligns well with the one documented in the literature [42], with the asymmetry signal peaking at a nominal photon energy of 708.5 eV. Setting the FEL to this energy, we mapped the asymmetry ratio as a function of B_x/B_y, normalized to the FEL harmonic intensity. This resulted in the figure of merit displayed in Fig. 4(b). The data indicate that the optimal B_x/B_y ratio is ∼0.29, aligning well with the qualitative estimate derived from the method outlined in the previous section. The L-edge resolved hysteresis loops, acquired by scanning the magnetic field applied to the sample, see Fig. 4(c), confirm the magnetic sensitivity of the produced radiation.

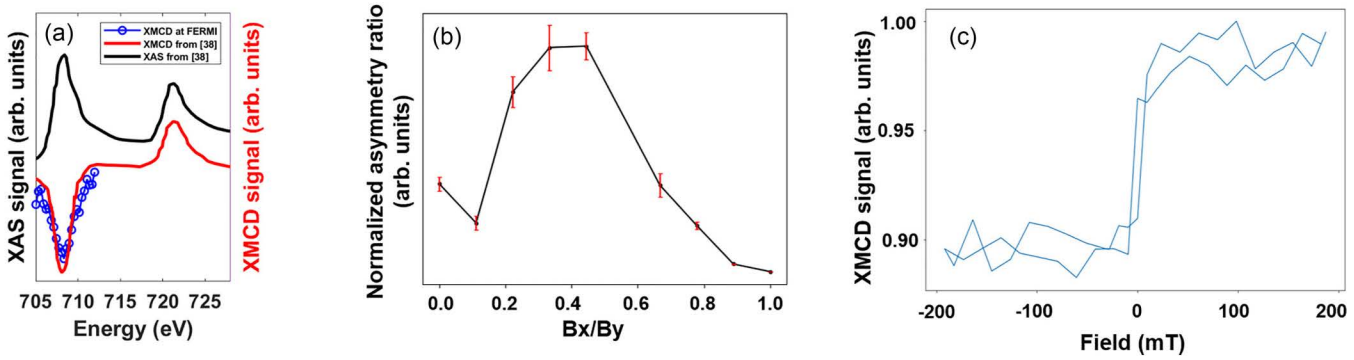

FIG. 4. (a) Asymmetry ratio obtained by scanning the radiation energy across the Fe-L_3 absorption edge (average over three independent measurements). For comparison purposes, we also show the dichroic contrast obtained in Ref. [42] through x-ray magnetic circular dichroism (XMCD) as well as the absorption edge spectrum obtained with x-ray absorption spectroscopy, on a $Ni_{72}Fe_{18}Gd_{10}$ sample, utilizing synchrotron circularly polarized light. (b) Asymmetry ratio as a function of B_x/B_y, normalized to the free-electron laser (FEL) intensity. (c) Example of L-edge resolved hysteresis loop measured at the Fe-L_3 edge, acquired by scanning the magnetic field applied to the sample.

These results demonstrate the possibility of using FEL harmonics with elliptical polarization to perform a selective characterization of the static properties of magnetic materials through circular dichroism.

B. Evolution of dichroic contrast measured by XRMS

The static and out-of-equilibrium properties of the texture of a SAFM, specifically a Pt/CoFeB/Ru multilayer of period d, were investigated via XRMS at the Fe-L_3 edge. The experiment took place at the DiProi beamline of the FERMI FEL [43,44], and the experimental setup is sketched in Fig. 5(a). In specular geometry, the exchanged momentum along z, the normal to the sample surface, is $q_z = 4\pi \sin(\theta_{\text{in}})/\lambda$, where λ is the wavelength of the incoming radiation, and θ_{in} is the (grazing) angle of incidence. Here, $\theta_B = a\sin(\lambda/2d)$ is the angle satisfying the Bragg condition ($q_z = 2\pi/d$) for specular reflectivity from the multilayer structure. Since the period of the antiferromagnetic (AFM) order is twice that of the multilayer, the corresponding Bragg condition ($q_z = 2\pi/2d$) is satisfied for an incidence angle $\theta_{\text{AFM}} \approx \theta_B/2$.

The experiment involved the combination of a 50 fs (full width at half maximum) infrared laser pump beam (at 780 nm) and x-ray probe beam of similar duration, provided by the FEL harmonic. The harmonic beam was obtained by setting the B_x/B_y ratio in the last two radiators to 0.29 for elliptical left (EL) and to -0.29 for elliptical right (ER) polarizations, as determined in the previous section.

As shown in Ref. [45], XRMS can address the magnetic properties of the SAFM, i.e., the existence of a chiral spin-spiral magnetic texture, when the incidence angle is tuned to match the AFM period. As described in more detail in Ref. [46], in the case of negligible perpendicular magnetic anisotropy, the origin of the spiral chiral texture is due by the balance of the Ruderman-Kittel-Kasuya-Yoshida AFM dipolar coupling and the interfacial Dzyaloshinskii-Moriya interaction. Figures 5(b) and 5(c) illustrate, respectively, the magnetic (EL + ER) and the chiral (EL − ER) signals obtained from diffraction patterns, captured using a CCD. This was done at $\theta_{\text{in}} = \theta_{\text{AFM}}$ for a negative pump-probe delay, providing insight into the unpumped (static) sample state. The CCD images of the diffused scattering collected as a function of $(\varphi, \Delta\theta)$ around the specular direction [Fig. 5(a)] are rescaled in terms of the exchanged momentum components in the detector plane $q_x = (4\pi/\lambda) \cdot \sin(\Delta\theta/2) \cdot \cos(\varphi)$ and $q_y = (4\pi/\lambda) \cdot \sin(\Delta\theta/2) \cdot \sin(\varphi)$, parallel to the sample surface. The obtained data closely match those from the experiment described in Ref. [45], conducted at SOLEIL synchrotron radiation source, which can be assumed to exhibit a circular polarization rate ∼100%. Such an experiment was performed on the same sample and under similar conditions as those discussed here.

The very good data quality allows us to estimate the degree of harmonic circular polarization with a high level of accuracy. For this purpose, we measured the θ dependence of the diffused scattering and chiral intensities around the θ_{AFM} scattering condition. Figures 6(a) and 6(b) show, respectively, the magnetic and chiral signals as a function of θ_{in}, while Fig. 6(c) shows the dichroic contrast (EL − ER)/(EL + ER). A direct inspection of Fig. 6(c) reveals a maximum contrast of ∼6.5%. A similar study was carried out at SOLEIL, obtaining a contrast of ∼15%. By employing a simple linear scaling, we can therefore estimate the degree of circular polarization of the FEL harmonic pulses to be ∼43%, a value aligning well with the one corresponding to $B_x/B_y = 0.29$ in Fig. 2(a).

The short duration and stability of the pulses produced by FERMI also allows the time response of the dichroism of the sample to be examined on a femtosecond time scale. Figure 5 also shows a sequence of representative snapshots of the spin dynamics at various delay times, after IR excitation. Following optical excitation (pump-probe delay = 0.5 ps) and comparing with the static case of Figs. 5(b) and 5(c), one can observe in Figs. 5(d) and 5(e) the expected effect of magnetization quenching and reduction of chiral contrast. On the longer time scale (18 ps) of Figs. 5(f) and 5(g), the system recovers toward its ground state. A more quantitative analysis of the spin and chiral texture dynamics is reported in Figs. 5(h) and 5(i), where the radial average of the total intensity as a function of the exchanged momentum and the azimuthal angle dependence of spin-spiral texture signal are shown, respectively, for different pump-probe delays. Figure 5(h) shows that, despite the reduction of

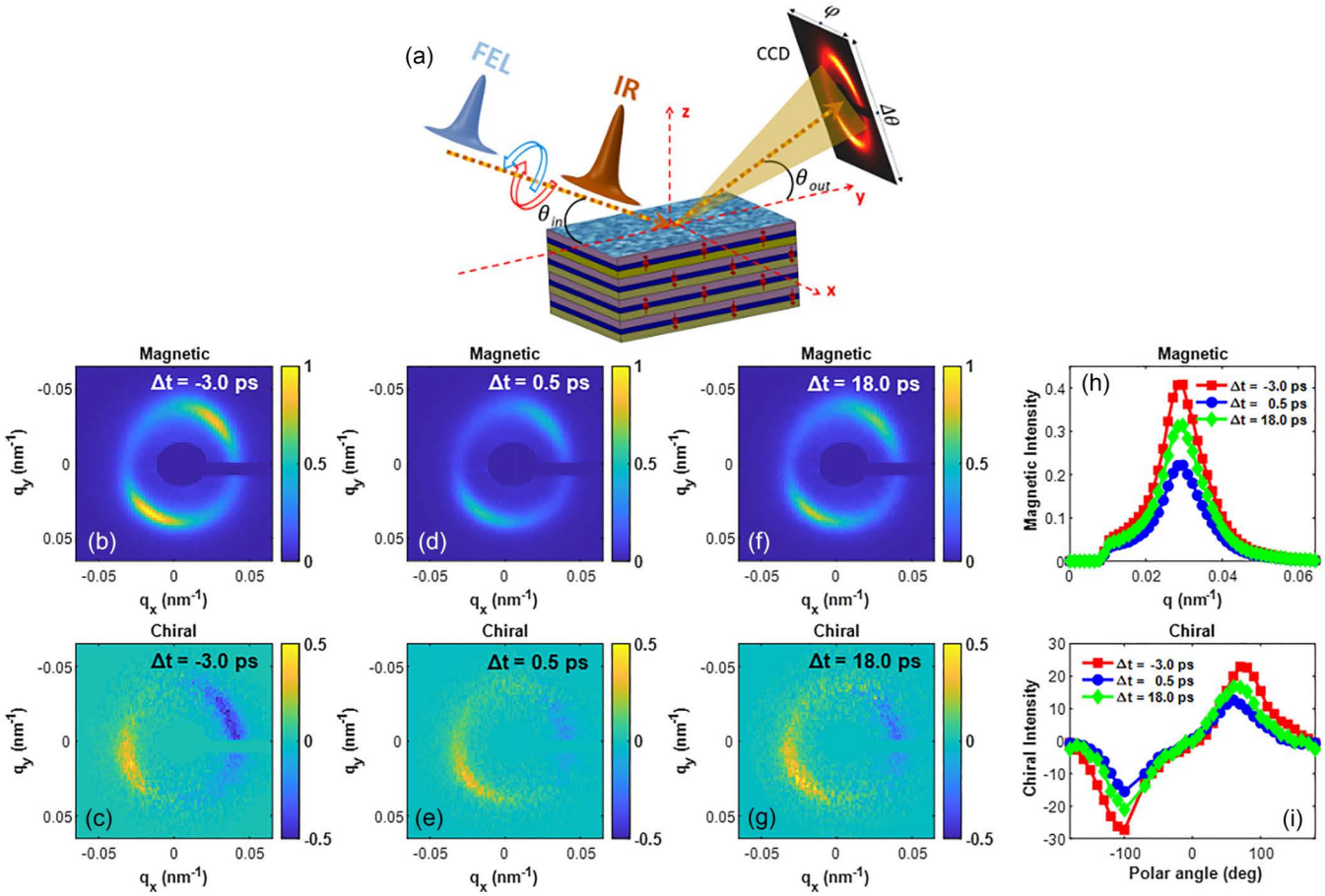

FIG. 5. (a) Setup of the experiment carried out at the DiProi station. A Pt(8 nm)/[$Co_{0.4}Fe_{0.4}B_{0.2}$(0.9 nm)/Ru(0.75 nm)/Pt(0.5 nm)]$_6$/Al(5 nm) magnetic multilayer structure is studied in reflection geometry, at an incidence angle defined by the Bragg condition. To trigger the spin dynamics, an infrared (IR) pump beam is used to excite the structure, and the magnetic evolution is probed by the delayed free-electron laser (FEL) harmonic beam, carrying either elliptical right (ER) or elliptical left (EL) polarization. The scattered photons, filtered by a Cu film to attenuate low-energy undesired radiation, are collected by means of a charge-coupled device (CCD) detector, located at ∼140 mm from the sample. (b), (d), and (f) Magnetic scattering signal (EL + ER), acquired at $\theta_{in} = \theta_{AFM}$ for different delays (i.e., −3, 0.5, and 18 ps) between the pump and the probe beams. (c), (e), and (g) Chiral signal (EL − ER) acquired at $\theta_{in} = \theta_{AFM}$ for different delays (−3.0, 0.5, and 18.0 ps). (h) Azimuthal average of (b), (d), and (f) showing the dependence of magnetic scattered intensity on the exchanged scattering momentum for the three selected time delays. Red curve: unperturbed static condition ($t = -3.0$ ps). Blue curve: reduced magnetic intensity after pump excitation ($t = 0.5$ ps). Green curve: long-term recovery of the magnetic contrast ($t = 18$ ps). (i) Azimuthal angular dependence of magnetically scattered photons in the exchanged momentum interval [0.02, 0.06] nm^{-1} of the chiral signal reported in (c), (e), and (g) at the same three delays as in (h). For each ellipticity, a diffraction pattern of 3000 FEL shots (60 s acquisition time) was collected on a CCD detector placed at a distance of ∼140 mm from the interaction point. The dynamics of the sample was triggered by a laser pulse focused on 350 × 350 μm^2 spot size, depositing on the sample surface an energy density of ∼6.5 mJ/cm^2. The estimated probe beam energy at the sample position was ∼3 nJ per pulse.

magnetic scattering intensity after the optical excitation, the maximum of magnetically scattered photons remains located at $\sim 0.033\,\mathrm{nm}^{-1}$. This confirms that the spin-spiral period (∼190 nm) is rather stable after excitation, in agreement with the temperature-dependence study reported in Ref. [46]. Furthermore, the unperturbed line shape of the azimuthal profile, as shown in Fig. 5(i), validates the preservation of the Néel-like nature of the spin-spiral chiral order throughout the spin dynamics. This is observed in conjunction with a reduction in the relative chiral contrast, attributed to the demagnetization process.

Overall, the reported results demonstrate that NHG-FEL elliptically polarized beams are well suited for element-selective time-resolved studies of the magnetic properties of complex systems via soft x-ray circular dichroism and resonant scattering.

IV. CONCLUSIONS

We have demonstrated the possibility to produce soft x-ray light pulses with a high degree of circular polarization by means of the harmonics generated by a seeded FEL. Such light, which maintains the high spatial and temporal coherence characteristics of seeded FELs and presently possesses unique properties, can be used for static and time-resolved experiments at the L edge of transition metal atoms. Therefore, in this paper, we pave the way to widening the range of experiments that can be performed at a seeded FEL source. This

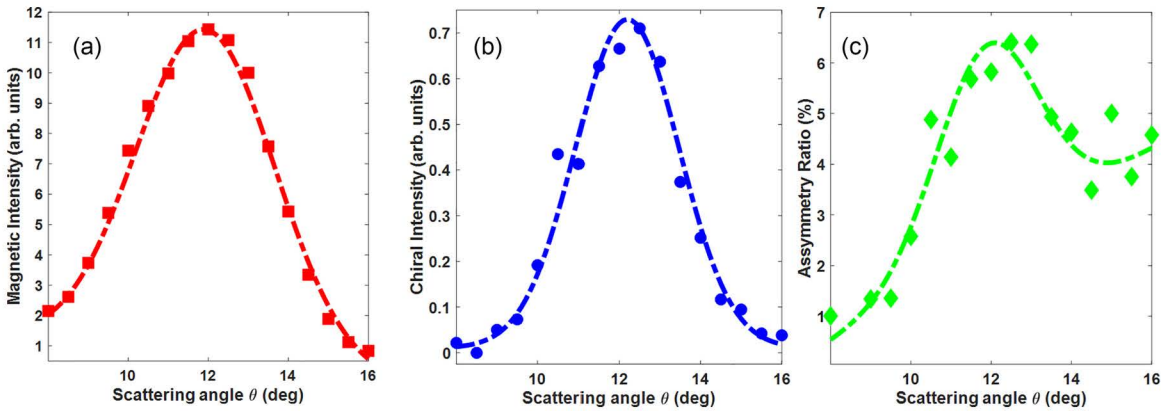

FIG. 6. (a) Dependence of the static magnetic scattering signal, defined as the total area of the scattered photons in Fig. 5(b), as a function of the free-electron laser (FEL) incidence angle. The data show an optimum of magnetic scattering of photons around 12 °, corresponding to θ_{AFM}. (b) Static chiral contrast dependence, defined as the total area of the scattered photons in Fig. 5(c), as a function of the FEL incidence angle. (c) Normalized asymmetry calculated as the ratio between the data in (b) and (a). Dashed lines in (a)–(c) are the combination of a Gaussian fit profile superimposed to a linear background, as a guide for the eyes.

includes extending Fourier transform holography to shorter wavelengths and improving imaging resolution [47] as well as to performing spectroscopic studies of spin dynamics and topology [48–50] that involve the combination of electronic levels with different excitation lifetimes, both at the *M* and *L* edges of transition metal atoms.

ACKNOWLEDGMENTS

N.J. and M.S. acknowledge funding from ANR under Grant No. ANR-20-CE42-0012 (MEDYNA). This paper received support from the GoToXFEL programme of CNRS (France).

[1] F. Meier and D. Pescia, Band-structure investigation of gold by spin-polarized photoemission, Phys. Rev. Lett. **47**, 374 (1981).

[2] *Photoemission in Solids II*, edited by M. Cardona and L. Ley, Topics in Applied Physics Vol. 27 (Springer, Berlin, 1979).

[3] *X-Ray and Neutron Reflectivity: Principles and Applications*, edited by J. Daillant and A. Gibaud (Springer, New York, 1999).

[4] P. Carra, M. Altarelli, and F. de Bergevin, Resonant exchange scattering of x rays in ferromagnetic systems, Phys. Rev. B **40**, 7324 (1989).

[5] J. C. Sutherland, E. J. Desmond, and P. Z. Takacs, Versatile spectrometer for experiments using synchrotron radiation at wave-lengths greater than 100 nm, Nucl. Instrum. Methods **172**, 195 (1980).

[6] R. W. Schoenlein, S. Chattopadhyay, H. Chong, T. E. Glover, P. Heimann, C. V. Shank, and M. Zolotorev, Generation of femtosecond pulses of synchrotron radiation, Science **287**, 2237 (2000).

[7] T. Kachel, K. Holldack, S. Khan, R. Mitzner, T. Quast, C. Stamm, and H. Duerr, Soft x-ray beamline for fs pulses from the BESSY fs-slicing source, AIP Conf. Proc. **879**, 1250 (2007).

[8] F. Willems, C. Smeenk, N. Zhavoronkov, O. Kornilov, I. Radu, M. Schmidbauer, and S. Eisebitt, Probing ultrafast spin dynamics with high-harmonic magnetic circular dichroism spectroscopy, Phys. Rev. B **92**, 220405 (2015).

[9] D. Schick, M. Borchert, W. Engel, C. von Korff Schmising, B. Pfau, and S. Eisebitt, X-ray magnetic circular dichroism spectroscopy at the Fe *L* edges with a picosecond laser-driven plasma source, Optica **10**, 450 (2023).

[10] R. Neutze, R. Wouts, D. van der Spoel, E. Weckert, and J. Hajdu, Potential for biomolecular imaging with femtosecond x-ray pulses, Nature (London) **406**, 752 (2000).

[11] N. Gedik, D. Yang, G. Logvenov, I. Božović, and A. H. Zewail, Nonequilibrium phase transitions in cuprates observed by ultrafast electron crystallography, Science **316**, 425 (2007).

[12] A. L. Cavalieri, N. Müller, T. Uphues, V. S. Yakovlev, A. Baltuška, B. Horváth, and U. Heinzmann, Attosecond spectroscopy in condensed matter, Nature (London) **449**, 1029 (2007).

[13] H. N. Chapman, S. P. Hau-Riege, M. J. Bogan, S. Bajt, A. Barty, S. Boutet, and J. Hajdu, Femtosecond time-delay x-ray holography, Nature (London) **448**, 676 (2007).

[14] S. Pathak, L. M. Ibele, R. Boll, C. Callegari, A. Demidovich, B. Erk, and D. Rolles, Tracking the ultraviolet-induced photochemistry of thiophenone during and after ultrafast ring opening, Nat. Chem. **12**, 795 (2020).

[15] H. N. Chapman, A. Barty, M. J. Bogan, S. Boutet, M. Frank, S. P. Hau-Riege, and J. Hajdu, Femtosecond diffractive imaging with a soft-x-ray free-electron laser, Nat. Phys. **2**, 839 (2006).

[16] F. Bencivenga, R. Cucini, F. Capotondi, A. Battistoni, R. Mincigrucci, E. Giangrisostomi, and C. Masciovecchio, Four-wave mixing experiments with extreme ultraviolet transient gratings, Nature (London) **520**, 205 (2015).

[17] B. Pfau, S. Schaffert, L. Müller, C. Gutt, A. Al-Shemmary, F. Büttner, and S. Eisebitt, Ultrafast optical demagnetization manipulates nanoscale spin structure in domain walls, Nat. Commun. **3**, 1100 (2012).

[18] H. N. Chapman, P. Fromme, A. Barty, T. A. White, R. A. Kirian, A. Aquila, and J. C. H. Spence, Femtosecond x-ray protein nanocrystallography, Nature (London) **470**, 73 (2011).

[19] T. E. Glover, D. Fritz, M. Cammarata, T. K. Allison, S. Coh, J. M. Feldkamp, and J. B. Hastings, X-ray and optical wave mixing, Nature (London) **488**, 603 (2012).

[20] E. Allaria, B. Diviacco, C. Callegari, P. Finetti, B. Mahieu, J. Viefhaus, and L. Giannessi, Control of the polarization of a vacuum-ultraviolet, high-gain, free-electron laser, Phys. Rev. X **4**, 041040 (2014).

[21] G. Perosa, J. Wätzel, D. Garzella, E. Allaria, M. Bonanomi, M. B. Danailov, and P. R. Ribič, Femtosecond polarization shaping of free-electron laser pulses, Phys. Rev. Lett. **131**, 045001 (2023).

[22] M. Pancaldi, C. Strüber, B. Friedrich, E. Pedersoli, D. D. Angelis, I. Nikolov, and F. Capotondi, The comix polarimeter: A compact device for XUV polarization analysis, J. Synchrotron Radiat. **29**, 969 (2022).

[23] A. Caretta, S. Laterza, V. Bonanni, R. Sergo, C. Dri, G. Cautero, and M. Malvestuto, A novel free-electron laser single-pulse wollaston polarimeter for magneto-dynamical studies, Struct. Dyn. **8**, 034304 (2021).

[24] J. M. J. Madey, Stimulated emission of bremsstrahlung in a periodic magnetic field, J. Appl. Phys. **42**, 1906 (1971).

[25] L. Yu, M. Babzien, I. Ben-Zvi, L. F. DiMauro, A. Doyuran, W. Graves, and I. Vasserman, High-gain harmonic-generation free-electron laser, Science **289**, 932 (2000).

[26] J. Murphy, C. Pellegrini, and R. Bonifacio, Collective instability of a free electron laser including space charge and harmonics, Opt. Commun. **53**, 197 (1985).

[27] Z. Huang and K. Kim, Three-dimensional analysis of harmonic generation in high-gain free-electron lasers, Phys. Rev. E **62**, 7295 (2000).

[28] A. Tremaine, X. J. Wang, M. Babzien, I. Ben-Zvi, M. Cornacchia, H. Nuhn, and V. Yakimenko, Experimental characterization of nonlinear harmonic radiation from a visible self-amplified spontaneous emission free-electron laser at saturation, Phys. Rev. Lett. **88**, 204801 (2002).

[29] G. Penco, G. Perosa, E. Allaria, L. Badano, F. Bencivenga, A. Brynes, and G. D. Ninno, Nonlinear harmonics of a seeded free-electron laser as a coherent and ultrafast probe to investigate matter at the water window and beyond, Phys. Rev. A **105**, 053524 (2022).

[30] M. J. Schmitt and C. Elliott, Even-harmonic generation in free-electron lasers, Phys. Rev. A **34**, 4843 (1986).

[31] G. Geloni, E. Saldin, E. Schneidmiller, and M. Yurkov, Theory of nonlinear harmonic generation in free-electron lasers with helical wigglers, Nucl. Instrum. Methods Phys. Res. A **581**, 856 (2007).

[32] E. Allaria, F. Curbis, M. Coreno, M. B. Danailov, B. Diviacco, C. Spezzani, and G. D. Ninno, Experimental characterization of nonlinear harmonic generation in planar and helical undulators, Phys. Rev. Lett. **100**, 174801 (2008).

[33] E. Allaria, G. D. Ninno, G. Geloni, and C. Spezzani, Angular distribution of nonlinear harmonic generation in helical undulators: A comparison between experiments and theory, Nucl. Instrum. Methods Phys. Res. A **654**, 575 (2011).

[34] C. Spezzani, E. Allaria, M. Coreno, B. Diviacco, G. Geloni, E. Karantzoulis, and G. D. Ninno, Coherent light with tunable polarization from single-pass free-electron lasers, Phys. Rev. Lett. **107**, 084801 (2011).

[35] G. D. Ninno, E. Allaria, M. Coreno, F. Curbis, M. B. Danailov, E. Karantzoulis, and M. Trovò, Generation of ultrashort coherent vacuum ultraviolet pulses using electron storage rings: A new bright light source for experiments, Phys. Rev. Lett. **101**, 053902 (2008).

[36] E. Allaria, D. Castronovo, P. Cinquegrana, P. Craievich, M. D. Forno, M. B. Danailov, and M. Zangrando, Two-stage seeded soft-x-ray free-electron laser, Nat. Photon. **7**, 913 (2013),.

[37] A. Doyuran, M. Babzien, T. Shaftan, L. Yu, L. F. DiMauro, I. Ben-Zvi, and I. Vasserman, Characterization of a high-gain harmonic-generation free-electron laser at saturation, Phys. Rev. Lett. **86**, 5902 (2001).

[38] S. Yamamoto and H. Kitamura, Generation of quasi-circularly polarized undulator radiation with higher harmonics, Jpn. J. Appl. Phys. **26**, L1613 (1987).

[39] H. G. Berry, G. Gabrielse, and A. E. Livingston, Measurement of the stokes parameters of light, Appl. Opt. **16**, 3200 (1977).

[40] R. P. Walker, Insertion devices: Undulators and wigglers, Proceedings CERN Accelerator School 98-04 (1998).

[41] M. Malvestuto, A. Caretta, R. Bhardwaj, S. Laterza, F. Parmigiani, A. Gessini, and M. Zangrando, The MagneDyn beamline at the Fermi free electron laser, Rev. Sci. Instrum. **93**, 115109 (2022).

[42] G. Boero, S. Rusponi, P. Benčok, R. Meckenstock, J. Thiele, F. Nolting, and P. Gambardella, Double-resonant x-ray and microwave absorption: Atomic spectroscopy of precessional orbital and spin dynamics, Phys. Rev. B **79**, 224425 (2009).

[43] F. Capotondi, E. Pedersoli, N. Mahne, R. Menk, G. Passos, L. Raimondi, and G. Grübel, Invited article: Coherent imaging using seeded free-electron laser pulses with variable polarization: First results and research opportunities, Rev. Sci. Instrum. **84**, 051301 (2013).

[44] F. Capotondi, E. Pedersoli, F. Bencivenga, M. Manfredda, N. Mahne, L. Raimondi, and M. Kiskinova, Multipurpose end-station for coherent diffraction imaging and scattering at FERMI@Elettra free-electron laser facility, J. Synchrotron Radiat. **22**, 544 (2015).

[45] C. Léveillé, S. Flewett, E. Burgos-Parra, Y. Sassi, W. Legrand, F. Ajejas, and N. Jaouen, Chiral spin spiral in synthetic antiferromagnets probed by circular dichroism in x-ray resonant magnetic scattering, Phys. Rev. B **104**, L060402 (2021).

[46] W. Legrand, D. Maccariello, F. Ajejas, S. Collin, A. Vecchiola, K. Bouzéhouane, and A. Fert, Room-temperature stabilization of antiferromagnetic skyrmions in synthetic antiferromagnets, Nat. Mater. **19**, 34 (2019).

[47] C. V. K. Schmising, B. Pfau, M. Schneider, C. Günther, M. Giovannella, J. Perron, and S. Eisebitt, Imaging ultrafast demagnetization dynamics after a spatially localized optical excitation, Phys. Rev. Lett. **112**, 217203 (2014).

[48] W. Legrand, J. Chauleau, D. Maccariello, N. Reyren, S. Collin, K. Bouzéhouane, and A. Fert, Hybrid chiral domain walls and skyrmions in magnetic multilayers, Sci. Adv. **4**, eaat0415 (2018).

[49] M. Grelier, F. Godel, A. Vecchiola, S. Collin, K. Bouzéhouane, V. Cros, and F. Büttner, X-ray holography of skyrmionic cocoons in aperiodic magnetic multilayers, Phys. Rev. B **107**, L220405 (2023).

[50] J. Chauleau, T. Chirac, S. Fusil, V. Garcia, W. Akhtar, J. Tranchida, and M. Viret, Electric and antiferromagnetic chiral textures at multiferroic domain walls, Nat. Mater. **19**, 386 (2019).